Available online at www.sciencedirect.com
SCIENCE DIRECT®
Journal of Sound and Vibration 293 (2006) 335–359
JOURNAL OF SOUND AND VIBRATION
www.elsevier.com/locate/jsvi

Robust and high precision control using piezoelectric actuator circuit and integral continuous sliding mode control design

X. Xue, J. Tang*

Department of Mechanical Engineering, The University of Connecticut, 191 Auditorium Road, Unit 3139, Storrs, CT 06269, USA

Received 9 February 2005; received in revised form 14 September 2005; accepted 4 October 2005
Available online 27 December 2005

Abstract

While piezoelectric actuators have been widely used in vibration suppression and high precision controls, their intrinsic nonlinearity such as hysteresis, if not considered in control design, may deteriorate the system performance. In this research, a new methodology is proposed for the high-precision and robust control using piezoelectric actuator with hysteresis compensation. This methodology is featured by the introduction of a resistance/inductance circuit connected to the piezoelectric actuator to form an actuator network and a new integral continuous sliding mode control (ICSMC) algorithm. In addition to the well-known increased passive damping and active control authority, the main advantage of the actuator network in this particular study is that the charge and/or current in the piezoelectric actuator now become independent state variables that can be directly measured and fed back. Not only can this actuator network configuration improve the hysteresis characterization, the control design can also be greatly simplified. With the introduction of the RL shunt circuit, two dynamic subsystems (the mechanical structure and the electrical circuit) are formed. With these two coupled dynamic subsystems as basis, we then develop an ICSMC scheme which combines the advantages of conventional continuous sliding mode control and integral variable structure control. Different from the inverse cancellation of hysteresis behavior which might not be reliable due to the measurement noise, a direct piezoelectric hysteresis compensation is achieved using this control strategy. Detailed analysis and case studies demonstrate that this new methodology can lead to improved precision for both tracking control and vibration attenuation, enhanced control robustness, and smoother control action.

1. Introduction

Because of their electromechanical coupling characteristics, piezoelectric materials have been widely utilized as actuators in such as vibration control and micro-positioning applications. Some advantages of piezoelectric actuators include high bandwidth, compactness, and easy integration. While high precision is oftentimes also claimed as one of the advantages, the performance of piezoelectric actuators in this regard is clearly dependent upon the modeling accuracy and control algorithms. Until recently, most of the studies related to piezoelectric actuators have been based upon a linear strain-field constitutive relation assumption. The presence of

*Corresponding author. Tel.: +1 (860) 486 5911; fax: +1 (860) 486 5088.
E-mail address: jtang@engr.uconn.edu (J. Tang).

0022-460X/$ - see front matter © 2005 Elsevier Ltd. All rights reserved.
doi:10.1016/j.jsv.2005.10.009

Nomenclature

A	cross section area	l_b, l_p	length
c_b	uniform beam damping constant	p	generalized electrical displacement
D	electrical displacement	Q	charge flow to the piezoelectric patch
E	electrical field	q	generalized mechanical displacement
E_b, E_p	Young's modulus	x_1,x_r	left and right ends of piezoelectric patch
h_p	thickness of piezoelectric patch	w_b, w_p	width
I	moment of inertia	ρ_b, ρ_p	density
		ϕ	beam first mode
		ψ	assumed mode for electrical displacement

nonlinearities in the response of piezoelectric materials, however, has been well documented since the early description of ferroelectrics [1]. The physics involved in piezoelectric theory may be regarded as a coupling between Maxwell's equations of electromagnetism and elastic stress equations of motion. The coupling takes place through the piezoelectric constitutive equations. Normally, in practical applications the electrical field (against the poling direction) applied to the piezoelectric actuator should be kept below the coercive field to avoid depoling. Moreover, experiments have revealed that even in cases where the applied fields are not sufficient to completely re-orient the remnant polarization in the entire actuator, a small number of domains can still be switched [2]. Thus, both the material states and the electro-mechanical coupling are changed, giving rise to the hysteretic strain-field behavior even at very low field level.

The hysteresis phenomenon obviously affects the piezoelectric control performance, and there has been recent interest in modeling such behavior [3–9]. In general, the hysteresis can be characterized by using the Preisach model [4–6] or its variant, the Maxwell resistive capacitor (MRC) model [7–9]. The Preisach model consists of a weighted summation of an infinite number of the simplest hysteresis operator (Fig. 1), each representing a rectangular loop in the input–output diagram. To avoid the amplification of measurement error in the classical Preisach model (CPM) that involves the differential operation, Ge and Jouaneh proposed a new calculation scheme, which is essentially a two-dimensional interpolation [5,6]. MRC model is composed of a number of elasto-slide elements connected in parallel (Fig. 2(b)). Each of these elements is subject to a Coulomb friction force. This model can represent the hysteresis relation between the force and displacement

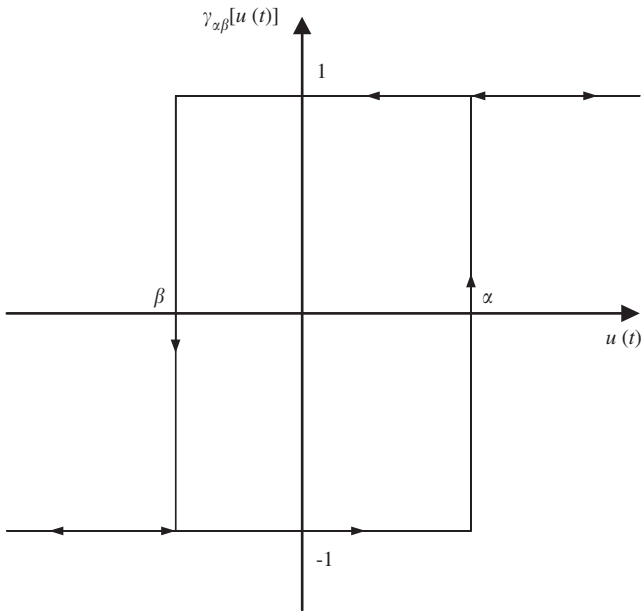

Fig. 1. The simplest hysteresis operator $\gamma_{\alpha\beta}$ is a rectangular loop with an up switch at α and a down switch at β.

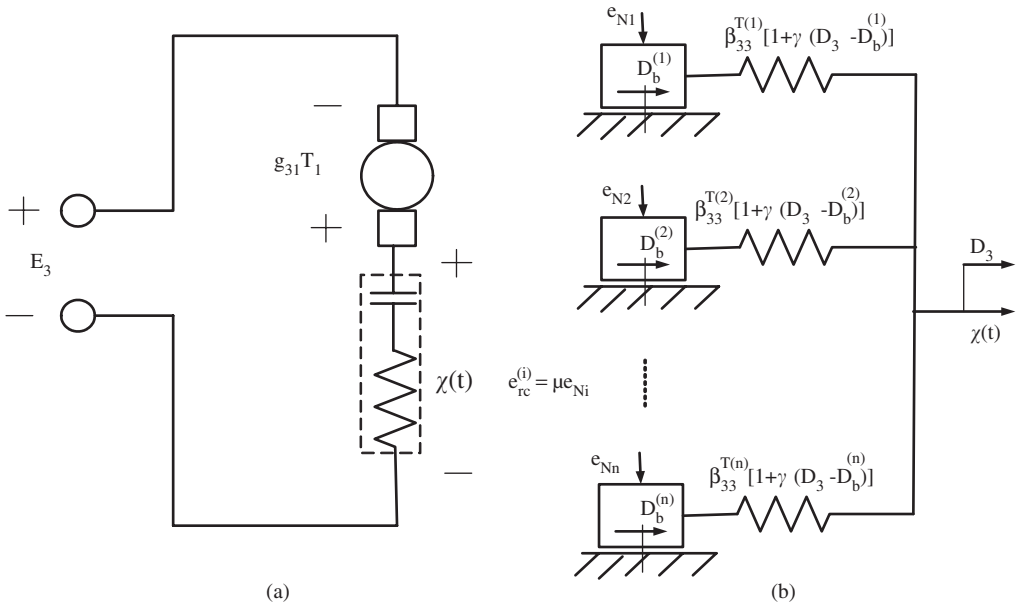

Fig. 2. Schematic representation of (MRC) hysteresis model: (a) equivalent electric circuit, (b) equivalent mechanical analogy.

[7–9]. Both Preisach model and MRC model, albeit complicated, can be used to accurately describe the piezoelectric hysteresis [4–9]. Researchers have also attempted to model the piezoelectric hysteresis behavior using polynomial approximation [10] and time delay process [11]. Following these modeling studies, several control strategies have been proposed to deal with the hysteresis nonlinearity involved in piezoelectric actuators, which include hysteresis cancellation using inverse model [12–15], feedback linearization [16], and Smith predictor [11]. Ge and Jouaneh proposed an inverse linearized Preisach model to offset the hysteresis of the piezoelectric actuator in the feedforward loop [12]. Similarly, based on a polynomial approximation of hysteresis effect, an inverse polynomial was developed by several researchers to cancel the hysteresis nonlinearity [13,15,17]. Kung and Fung developed a neural network based inverse hysteresis model [14]. Choi et al. employed a feedback linearization technique to deal with piezoelectric hysteresis and utilized a PID/repetitive controller to enhance the tracking performance [16]. Tsai and Chen used a Smith predictor to handle the time delay approximation of hysteresis, and an H_∞ controller is proposed to guarantee the robust tracking performance [11]. In these approaches, several factors may deteriorate the control performance. For example, very complex coupling effects exist among the stress, strain, electrical field, and electrical displacement of a piezoelectric actuator. Thus, the hysteretic strain-field relation of the actuator actually also depends on the electrical displacement/charge and stress which are typically treated as internal variables in the aforementioned control designs. The estimation of these internal variables and hence the characterization of hysteresis become extremely complicated and even unreliable in practical applications when the actuator is bonded to a host structure and thus also undergoes deformation. Moreover, the forward physical process (hysteresis) is usually an integral process, and in inverse modeling/cancellation methods, the differential operation will be involved in the hysteresis inverse calculation. As a result, the inverse model obtained may not be reliable when the hysteresis measurement data contains noise. It is worth noting that in all the hysteresis compensation approaches mentioned above, one will inevitably have a modeling error due to the inaccurate hysteresis modeling or its inverse and the un-modeled dynamics, etc. The control robustness, nevertheless, has not been sufficiently addressed in these hysteresis-related studies. Tang and Wang recently explored the piezoelectric robust control using a sliding mode theory, where the linear constitutive relation is used as the baseline and all nonlinearities are considered as uncertainties [18]. Such approach has not utilized the progress in hysteresis modeling, and is conservative in nature and may compromise the system control performance especially in high precision applications.

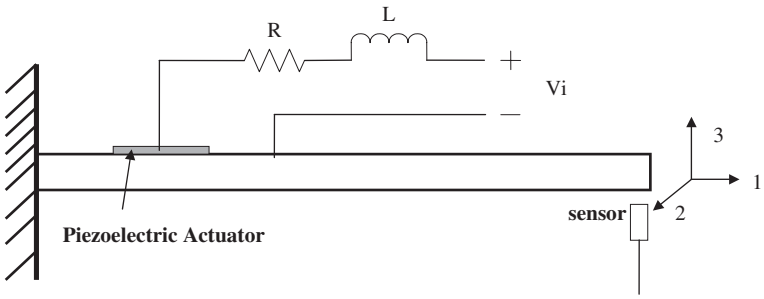

Fig. 3. Cantilevered beam with a piezoelectric actuator circuit.

In the present study, we develop a new methodology for the robust and high precision control using piezoelectric actuator with hysteresis compensation. The MRC model is employed to characterize the piezoelectric hysteresis, where experimental data from the open literature [9,19] are used. Without loss of generality, a cantilevered beam bonded with a piezoelectric actuator is used to illustrate the control strategy (Fig. 3). In this approach, a resistor/inductor (RL) shunt circuit is connected in series with the piezoelectric actuator to form an actuator network. In addition to the increased passive damping and active control authority [20], the main advantage of this actuator network is that the charge and/or current in the piezoelectric actuator now become independent state variables that can be directly measured and fed back. Not only can this actuator network configuration improve the hysteresis characterization accuracy, the control design can also be greatly simplified. With the introduction of the RL shunt circuit, the controlled system now consists of two coupled second-order *dynamic* subsystems, the mechanical subsystem and the electrical subsystem, whereas the nonlinearity only appears explicitly as a function of the electrical charge. This nonlinear dynamic system can be readily cast into the standard state-space form, and we then develop an integral continuous sliding mode control (ICSMC) which combines the advantages of conventional continuous sliding mode control (CSMC) [21] and integral variable structure control (IVSC) [22]. This approach can directly compensate the piezoelectric hysteretic nonlinearity. Detailed analysis and case studies demonstrate that this new methodology can lead to improved precision for both tracking control and vibration attenuation, enhanced control robustness, and smoother control action.

2. Hysteretic behavior of piezoelectric material and system modeling

Piezoelectric materials are ferroelectric, and their displacement responses to an applied electrical field are intrinsically nonlinear. The physical explanation of this phenomenon provided by Chen and Montgomery [23] shows that the effective number of dipoles aligned in the direction of the applied field changes over time as domains switch under the action of an external electric field. This essentially gives rise to the hysteresis behavior (Fig. 4).

2.1. Piezoelectric hysteresis characterization

The Preisach model basically is the continuous analog of a finite parallel connection of relays. Generally, two aspects of nonlinearities are involved in hysteretic behavior [4]: one is the hysteretic nonlinearity with local memory where the future output depends only on the future input; the other is the hysteretic nonlinearity with non-local memory where the future output depends not only upon the current output and future input but also on the past history of input switching values [5]. When used to describe the piezoelectric hysteresis, the CPM can be written as [4–6]

$$\chi(t) = \iint_{\alpha \geqslant \beta} \mu(\alpha, \beta)\gamma_{\alpha\beta}[u(t)]\,\mathrm{d}\alpha\,\mathrm{d}\beta, \tag{1}$$

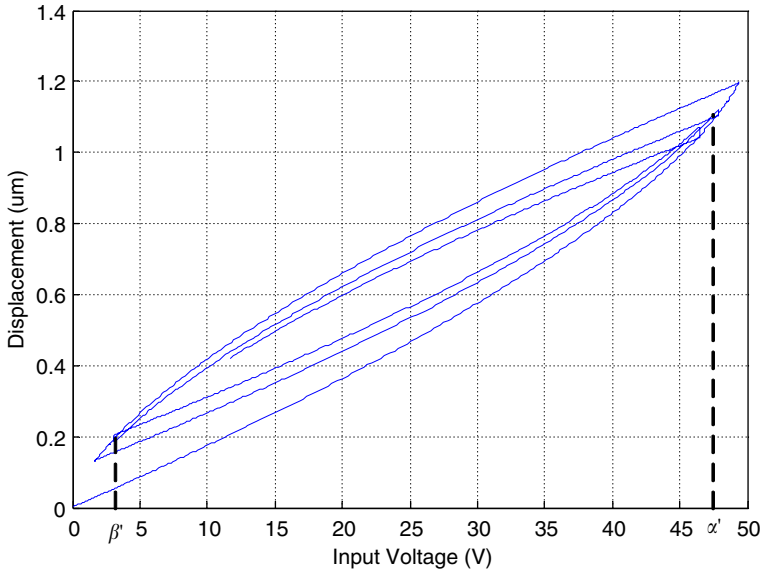

Fig. 4. Hysteresis loop of a piezoelectric actuator.

where $\chi(t)$ is the displacement response of the piezoelectric actuator, $u(t)$ is the input voltage, $\mu(\alpha, \beta)$ is a weighting function, $\gamma_{\alpha\beta}$ is the hysteresis relay operator whose value is determined by the input operation , and α and β represent "up" and "down" switching values of the input (Fig. 1). In order to calculate the displacement response, the weighting function $\mu(\alpha, \beta)$ needs to be known, which is traditionally calculated by differentiating the Preisach function $\Gamma(\alpha', \beta')$ in the following manner [5]:

$$\mu(\alpha', \beta') = -\frac{\partial^2 \Gamma(\alpha', \beta')}{\partial \alpha' \partial \beta'}, \tag{2}$$

where $\Gamma(\alpha', \beta')$, which can be obtained from experimental data, represents the change in the hysteresis loop of displacement response when the input voltage $u(t)$ changes from α'(orβ') to β'(or α') (Fig. 4). As the experimental data usually contains measurement noise, the differential operation in Eq. (2) will amplify the error. As a result, the model might not be reliable. To bypass the differential operation, Ge and Jouaneh proposed a new calculation scheme which is implemented through the two-dimensional interpolation using experimental data [5,6]. A typical hysteretic response under a decaying sinusoidal input excitation described by the CPM model is shown in Fig. 4. It is worth noting that the trajectory shows a jump (discontinuous point) at the switching point due to the interpolation variables switching from β (or α) to α (or β).

The hysteresis behavior can also be modeled using the MRC representation [7–9], which consists of a number of elasto-slide elements subject to Coulomb friction connected in parallel (Fig. 2(b)). If the element number becomes infinite, the model is referred to as generalized Maxwell slip. This model can be extended to its electrical analogy to represent the piezoelectric hysteresis behavior (Fig. 2(a)). By introducing a parameter γ to account for a reversible nonlinear stiffness effect (Fig. 2(b)), Lee and Royston extended the MRC model [9], which is represented as

$$\chi(t) = \sum_{i=1}^{n} E_{rc}^{(i)}, \tag{3a}$$

where

$$E_{rc}^{(i)} = \begin{cases} \beta_{33}^{\mathrm{T}(i)}[1 + \gamma(D_3 - D_b^{(i)})](D_3 - D_b^{(i)}), & \text{if } \left|\beta_{33}^{\mathrm{T}(i)}[1 + \gamma(D_3 - D_b^{(i)})](D_3 - D_b^{(i)})\right| < e_{rc}^{(i)}, \\ e_{rc}^{(i)}\mathrm{sgn}[\dot{D}_3] \text{ and } D_b^{(i)} \text{ is subject to } \left|\beta_{33}^{\mathrm{T}(i)}[1 + \gamma(D_3 - D_b^{(i)})](D_3 - D_b^{(i)})\right| = e_{rc}^{(i)} & \text{otherwise.} \end{cases} \tag{3b}$$

Correspondingly, β_{33}^{T}, e_N, μ, e_{rc} and D_b are, respectively, the electrical analogies to the mechanical spring stiffness, normal force, Coulomb friction coefficient, Coulomb friction force, and the displacement from the equilibrium position of a massless box (Fig. 2(b)). Here n is the number of massless boxes.

Both CPM and MRC have been successfully utilized for the modeling of piezoelectric hysteresis [5–9]. It is worth mentioning that the new control strategy developed in this research does not particularly depend upon a specific hysteresis model, i.e., either CPM (Eq. (1)) or MRC (Eq. (3)) or other hysteresis models can be inserted into the control design. Without loss of generality, in what follows we use MRC to demonstrate the control design.

2.2. Nonlinear dynamic model of a cantilevered beam integrated with a piezoelectric actuator circuit

The purpose of this paper is to develop a new control strategy for the robust and high precision control using piezoelectric actuator with hysteresis compensation. To illustrate the system development, we use a cantilevered beam as an example for control design (Fig. 3). The control objective could be tracking control or vibration suppression. For the beam problem, the following linear piezoelectric constitutive relation has been widely used [24]:

$$S_1 = s_{11}^{D} T_1 + g_{31} D_3, \quad E_3 = -g_{31} T_1 + \beta_{33}^{T} D_3, \tag{4a,b}$$

where "1" is the longitudinal direction, "2" the width direction, "3" the transversal direction (Fig. 3), S the strain, T the stress, D the electrical displacement, and E the electrical field [24]. Here it is usually assumed that the stress components at the beam width direction and at the transversal direction are both zero, and the in-plane components of the electrical displacement and electrical field are all zero, i.e., $T_3 = T_2 = D_1 = D_2 = E_1 = E_2 = 0$. It is well known that the electrical field (against the poling direction) applied to the piezoelectric actuator should be kept below the coercive field to avoid depoling. Recent studies have revealed, however, that even in cases that the applied fields are not sufficient to completely re-orient the remnant polarization in the entire actuator, a small number of domains can still be switched. Thus, both the material states and the electro-mechanical coupling are changed, giving rise to the hysteretic strain-field behavior even at very low field level. A number of experimental observations show that the electrical displacement D and electrical field E exhibits a strong hysteretic behavior [7,9,19,25,26]. Under zero stress T, while the applied electrical displacement D versus strain S relation is reversible (without hysteresis), the applied electrical field E versus S is not. It has been identified that the mechanical stress–strain relation under constant electrical displacement is reversible, but this relation under constant electrical field is hysteretic [7]. In addition, the relation between the applied stress and the electrical displacement is hysteretic [27–29]. In order to account for all these characteristics, a nonlinear term should be introduced to the original linear constitutive relation [9]. It is worth mentioning that the Poisson's ratio of the piezoelectric actuator is generally different from that of the beam and, consequently, the stress component T_2 is not zero. Combining all above observations, we can get the following relation for a piezoelectric actuator [9]:

$$T_1 = \bar{c}_{11}^{D} S_1 - h_{31} D_3, \quad E_3 = -g_{31}(\bar{c}_{11}^{D} + \bar{c}_{12}^{D}) S_1 + 2h_{31} g_{31} D_3 + \{\beta_{33}^{T} D_3\}, \tag{5a,b}$$

where $\bar{c}_{11}^{D} = c_{11}^{D} - v_p c_{13}^{D}$ and $\bar{c}_{12}^{D} = c_{12}^{D} - v_p c_{23}^{D}$, and the Poisson's ratio of the piezoelectric material is $v_p = -S_3/S_1$. In Eq. (5b), $\{\}$ is the hysteresis operator and $\{\beta_{33}^{T} D_3\}$ denotes the hysteresis effect, which can be either the MRC model, CPM model or other nonlinear models.

The mathematical model of a cantilevered beam integrated with a piezoelectric actuator is developed under the following assumptions: (1) the bonding between the beam and the piezoelectric actuator is perfect, i.e., the beam and the actuator have the same displacement at the bonding location; (2) the poling direction of the piezoelectric actuator is in the positive transversal direction of the beam; (3) the piezoelectric actuator is thin and short compared to the beam.

The system equations can then be derived using Hamilton's principle and the assumed mode method. In this study, we use a single mode, the dominant beam mode, for discretization. The transversal displacement of the beam can be expressed as

$$w(x, t) = \phi(x) q(t), \tag{6}$$

where ϕ is the first mode of the cantilevered beam without the piezoelectric patch, and q is the generalized mechanical displacement. We can then obtain the system equations (see Appendix A for details)

$$m\ddot{q} + g\dot{q} + kq + k_1 Q = F_m, \quad k_2 Q + k_3 q + f(Q) = V_a, \tag{7a,b}$$

where m is the equivalent mass, q the generalized mechanical displacement, g the beam equivalent damping, k the equivalent stiffness, k_1 and k_3 the cross coupling coefficients, F_m the external disturbance force, Q the charge flow to the piezoelectric actuator, k_2 the inverse of capacitance of the piezoelectric actuator, h_p the actuator thickness, and V_a the voltage across the piezoelectric actuator. It is worth emphasizing that $f(Q) = h_p\{\beta_{33}^{\mathrm{T}} Q\}$ is a nonlinear function of Q and reflects the hysteresis behavior.

Observe Eqs. (7a,b) and note that the input voltage across the piezoelectric actuator is V_a. When the hysteresis effect $f(Q)$ is neglected, one can combine the mechanical (dynamic) Eq. (7a) and the electrical (static) Eq. (7b) together by eliminating the generalized electrical coordinate Q. The presence of piezoelectric hysteresis, however, rules out the possibility of mathematically eliminating Q. The main difficulty in developing a control algorithm for the nonlinear system described by Eqs. (7a,b) appears to be that the second equation is a static one that contains an extremely complicated nonlinear term that is possibly subjected to modeling error and uncertainties.

In literature, a variety of control approaches have been proposed to deal with the piezoelectric nonlinear behavior with different complexity of hysteresis models [10–17]. One approach is based upon the inverse hysteresis modeling in the feedforward controller, and a feedback is used to regulate the output error. Polynomial approximation and neural network were employed to model the inverse hysteresis [13–15,17]. Another approach used is the traditional feedback linearization [16]. Based on a time delay model, a Smith predictor is employed to compensate the hysteresis nonlinearity [11]. In these approaches, several factors may deteriorate the control performance. For example, the forward physical process (hysteresis) is usually an integral process, while in inverse modeling/cancellation methods the differential operation will be involved in the hysteresis inverse calculation. As a result, the inverse model obtained may not be reliable when the hysteresis measurement data contains noise. In addition, typical inverse design approach treats the hysteresis and structural dynamics separately, i.e., the hysteresis is decoupled from structural dynamics. Such separation, however, is difficult to achieve in the practical measurement of piezoelectric actuation. It is worth mentioning that most of the aforementioned approaches were developed for piezoelectric stack actuator where the motion of the actuator is along the poling direction. The case of piezoelectric patch actuator that is being discussed in this research generally has more complicated nonlinear coupling effect.

In this research, we propose a different approach for dealing with the piezoelectric hysteresis by introducing dynamics to the electrical part of the controlled system. Here we use the idea of shunting the piezoelectric actuator with an RL circuit [20,30], as shown in Fig. 3. The system equations then become (see Appendix A)

$$m\ddot{q} + g\dot{q} + kq + k_1 Q = F_m, \tag{8a}$$

$$L\ddot{Q} + R\dot{Q} + k_2 Q + k_3 q + f(Q) = V_i, \tag{8b}$$

where L and R are the inductance and resistance, respectively, and V_i is the control input. Observe Eqs. (8a) and (8b) and compare them with Eq. (7a,b). Cleary, the main advantage of introducing dynamics to the piezoelectric actuator is that the charge and/or current in the piezoelectric actuator now become independent state variables that can be directly measured and fed back [20,30]. Not only can this actuator network configuration improve the hysteresis characterization accuracy, the control design can also be greatly simplified. With the introduction of the RL shunt circuit, the controlled system now consists of two coupled second-order *dynamic* subsystems, the mechanical subsystem (8a) and the electrical subsystem (8b), whereas the nonlinearity only appears explicitly as a function of the electrical charge. As will be shown later, this nonlinear dynamic system can be readily cast into the standard state-space form, and one may then use various nonlinear control methods to handle the hysteresis problem. It should be noted that the aforementioned piezoelectric actuator network configuration has also shown improved passive damping and active control authority. Under the linear constitution relation assumption, one may find optimal resistance and inductance values for the maximum damping and/or active authority amplification [20,30].

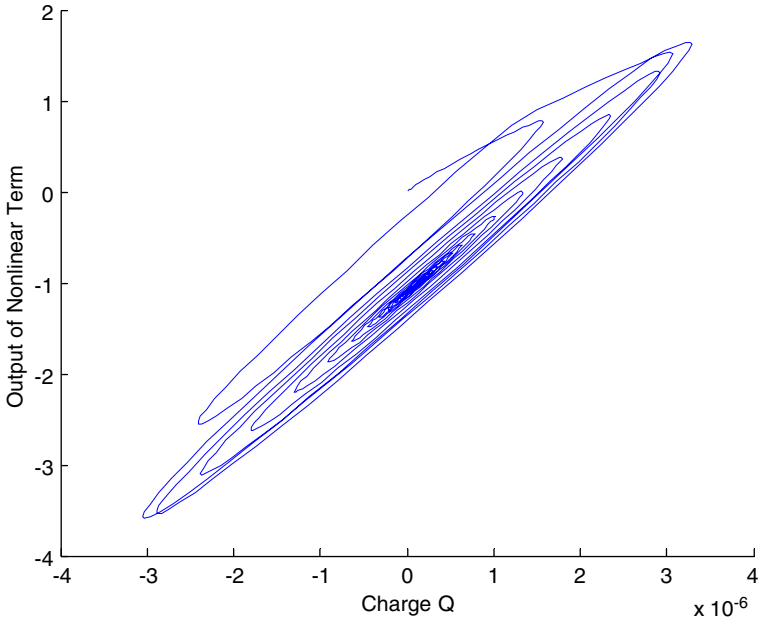

Fig. 5. Hysteresis behavior (MRC) of a piezoelectric actuator due to the free vibration of cantilever beam.

Table 1
MRC parameters of a monolithic piezoelectric actuator [8]

$\beta_{33}^{\mathrm{T}(i)} \times 10^{-6}$	0.30868	0.23188	0.18356	0.41700	1.67796
$e_{rc}^{(i)}$	0.08996	0.13515	0.16048	0.16529	∞

Table 2
System parameters used in simulation [8,18]

$l_b = 0.3\,\mathrm{m}$	$w_b = 0.0381\,\mathrm{m}$	$h_b = 0.003175\,\mathrm{m}$
$\rho_b = 7.8335 \times 10^3\,\mathrm{kg/m^3}$	$E_b = 1.9818 \times 10^{11}\,\mathrm{N/m^2}$	$C_b = 2.0576$
$w_p = 0.0343\,\mathrm{m}$	$h_p = 0.000267\,\mathrm{m}$	$x_l = 0.02\,\mathrm{m}$
$x_r = 0.0724\,\mathrm{m}$	$\rho_p = 7.8 \times 10^3\,\mathrm{kg/m^3}$	$E_p = 6.2 \times 10^{10}\,\mathrm{N/m^2}$
$h_{31} = -1.35 \times 10^9\,\mathrm{V/m}$	$g_{31} = -9.5 \times 10^{-3}\,\mathrm{Vm/N}$	$\bar{c}_{11}^{D} = 10.64 \times 10^{10}\,\mathrm{N/m^2}$
$\bar{c}_{12}^{D} = -5.68 \times 10^{10}\,\mathrm{N/m^2}$	$L = 76\,\mathrm{h}$	$R = 3090\,\Omega$

Throughout this paper, without loss of generality, the inductance L and resistance R are chosen in such a manner that they yield the maximum vibration damping/absorbing under passive situation [20].

The piezoelectric hysteresis effect $f(Q)$ in Eq. (8) (illustrated in Fig. 3) is demonstrated in Fig. 5, where an initial velocity is imposed on the tip of the beam with both external disturbance F_m and input voltage V_i being zero. Here we use the MRC model in the simulation, and all system parameters are listed in Tables 1 and 2.

3. Integral continuous sliding mode control (ICSMC) design

System (8) can be readily cast into the standard state-space form

$$\dot{x} = Ax - Bf(x_3) + Bu + DF_m, \tag{9}$$

where

$$x^{\mathrm{T}} = [x_1 \quad x_2 \quad x_3 \quad x_4]^{\mathrm{T}} = [q \quad \dot{q} \quad Q \quad \dot{Q}]^{\mathrm{T}}, \tag{10a}$$

$$A = \begin{bmatrix} 0 & 1 & 0 & 0 \\ -\frac{k}{m} & -\frac{g}{m} & -\frac{k_1}{m} & 0 \\ 0 & 0 & 0 & 1 \\ -\frac{k_3}{L} & 0 & -\frac{k_2}{L} & -\frac{R}{L} \end{bmatrix}, \tag{10b}$$

$$B^{\mathrm{T}} = \left[0, 0, 0, \frac{1}{L}\right]^{\mathrm{T}}, \quad D^{\mathrm{T}} = \left[0, \frac{1}{m}, 0, 0\right]^{\mathrm{T}}, \tag{10c,d}$$

where u represents the control input V_i. Its worth mentioning that all the system parameters are subject to uncertainties. In this paper, full state feedback is assumed. For system (9), various nonlinear control methods could be implemented. While the traditional feedback linearization technique is straightforward, parameter uncertainties of the system and modeling error/uncertainty on the hysteresis effect might deteriorate the control performance. In this study, we develop an ICSMC that is improved from conventional CSMC [21] and IVSC [22]. This method can directly deal with the hysteresis nonlinearity in forward cancellation, and also allows us to implement cubic state feedback which improves the system robustness as compared with IVSC.

The unique feature of the variable structure control is that the desired system dynamics with required performances (static and dynamic characteristics) can be designed using a sliding manifold [31,32]. The designed system dynamics is generally of lower order than the original system. Once the reduced order system with the sliding manifold is provided, a variable structure control action, which consists of the equivalent control action and the switching control action, is developed so that the switching control action constraints the system to follow the designed sliding manifold while the equivalent control action controls the performance of the reduced order dynamic system. Therefore, a typical variable structure control design consists of two modes, the reaching mode and the sliding mode [31,32]. For the reaching mode, the control action is to force the response of the system to reach the sliding manifold in finite time. Once it enters the sliding manifold, the response of the system will be constrained to follow the sliding manifold and approach the steady state. Consequently, the performances of the system will depend on not only the reaching mode but also the characteristics of the sliding manifold. One of the fundamental requirements of the sliding manifold definition is that the system dynamics should be stable and have robustness once it enters the sliding motion, so that the system can finally reach the zero point (the steady state of the system). While the traditional manifold design using linear combination of system states can meet certain performance requirement such as robust stability, it is difficult to satisfy the tracking performance when the system is required to follow a reference input signal [22,33]. The integral control (based on internal model principle), as an effective approach of eliminating errors, has been widely employed in tracking control [34]. The combination of integral control and variable structure control, which leads to the IVSC, was first proposed to control the electrohydraulic velocity servosystems [22], and then generalized to an MIMO system [33]. Essentially, the integral of the tracking error is used in the definition of the sliding manifold. On the other hand, the control action of traditional variable structure is discontinuous in nature due to the switching control at the reaching mode, which leads to the chattering phenomenon and in turn may trigger the high frequency un-modeled dynamics. To improve, Zhou and Fisher developed a CSMC [21]. This approach retains the positive properties such as robustness and disturbance rejection capability of traditional variable structure control, and in the meantime uses a continuous control law to completely eliminate the chattering problem on the other. However, this CSMC cannot be directly applied when the system is commanded to track a reference signal.

In what follows, we develop an ICSMC, which is a combination of CSMC and ISVC. This approach can directly deal with both the tracking problem and the hysteresis nonlinearity, which keeps the merits of CSMC such as robustness and continuous control action as long as the reference signal is continuous.

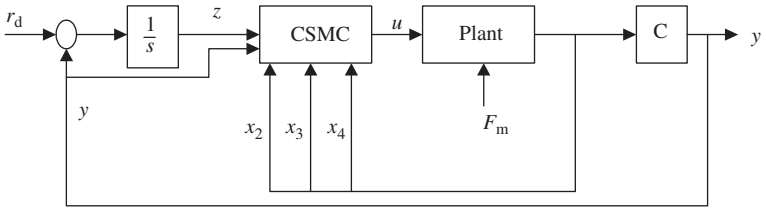

Fig. 6. Block diagram of ICSMC.

3.1. Determination of control action

We define

$$z = \int_0^t [r_d - \phi(l)x_1]\,\mathrm{d}t, \tag{11}$$

where r_d is the reference input signal, and l the beam length. Clearly, z indicates the tracking error between the command input signal and the actual beam tip displacement. The block diagram of the ICSMC to minimize z is shown in Fig. 6. We then define the sliding manifold as [22,33]

$$s = \sum_{i=1}^{4} c_i x_i + c_5 \int [r_d - \phi(l)x_1]\,\mathrm{d}t = C^{\mathrm{T}}x + c_5 \int [r_d - \phi(l)x_1]\,\mathrm{d}t \tag{12}$$

where $C = [c_1, c_2, c_3, c_4]^{\mathrm{T}}$. Essentially, the sliding manifold is a linear combination of the system states and the tracking error term.

In order to compensate the piezoelectric hysteresis and attenuate the external disturbance, here we propose the following control action for system (9):

$$u = -Kx + \hat{f}(x_3) - u_d, \tag{13}$$

where $K = [K_1, K_2, K_3, K_4]$ denotes state gain, $\hat{f}$ is the hysteresis estimation, and u_d is the disturbance rejection term. As will be shown later, this control action actually leads to a cubic state feedback. Therefore, once the states move away from the sliding manifold, the proposed ICSMC will provide more powerful control and faster reaction due to its cubic feedback nature. It is still worth mentioning that, following along the similar approach developed in Ref. [21] for nonlinear systems, one may end up with a feedback control that is of first or second order, which, in general, leads to less efficient control actions.

We now apply the reaching condition

$$s\dot{s} < 0. \tag{14}$$

Recalling Eqs. (13) and (9), and assuming $C^{\mathrm{T}}B \neq 0$ with a constant sign (e.g., $C^{\mathrm{T}}B > 0$), we obtain

$$s\dot{s} = s\{C^{\mathrm{T}}\dot{x} + c_5[r_d - \phi(l)x_1]\} = sC^{\mathrm{T}}B\{[\alpha - K]x + [\beta + \gamma c_5 r_d - u_d]\}, \tag{15}$$

where

$$\alpha = (C^{\mathrm{T}}B)^{-1}(C^{\mathrm{T}}A - A_\phi) = [\alpha_1, \alpha_2, \alpha_3, \alpha_4], \tag{16a}$$

$$\beta = (C^{\mathrm{T}}B)^{-1}C^{\mathrm{T}}DF_m + \Delta f, \quad \gamma = (C^{\mathrm{T}}B)^{-1}, \tag{16b,c}$$

$$A_\phi = [c_5\phi(l), 0, 0, 0], \quad \Delta f = \hat{f}(x_3) - f(x_3). \tag{16d,e}$$

Denote

$$\bar{\alpha}_i = \frac{\sup\ \alpha_i + \inf\ \alpha_i}{2}, \quad i = 1, 2, 3, 4 \tag{17}$$

$$\bar{\beta} = \frac{\sup\ \beta + \inf\ \beta}{2}, \quad \bar{\gamma} = \frac{\sup\ \gamma + \inf\ \gamma}{2}, \quad \bar{B} = \frac{\sup\ B + \inf\ B}{2}. \tag{18-20}$$

Using Eq. (20), we have

$$C^{\mathrm{T}}B = \varepsilon(C^{\mathrm{T}}\bar{B}), \quad 0 < \varepsilon \leqslant 1. \tag{21}$$

In order to satisfy the reaching condition (14), we may choose the control parameters

$$K_i = \bar{\alpha}_i + (\sup\ \alpha_i - \bar{\alpha}_i + \delta_i)\frac{sC^{\mathrm{T}}\bar{B}x_i}{\lambda}, \quad \delta_i > 0, \quad i = 1,2,3,4, \tag{22}$$

$$u_d = \bar{\beta} + \bar{\gamma}c_5 r_d + \{[\sup\ \beta - \bar{\beta}] + (\tilde{\gamma} - \bar{\gamma})c_5 r_d + \delta_d\}\frac{sC^{\mathrm{T}}\bar{B}}{\lambda}, \ \delta_d > 0, \tag{23}$$

where

$$\tilde{\gamma} = \begin{cases} \sup\ \gamma & \text{when } c_5 r_d > 0, \\ \inf\ \gamma & \text{when } c_5 r_d < 0 \end{cases} \tag{24}$$

and λ, δ_i ($i = 1,2,3,4$) and δ_d are design parameters. Indeed, λ is the boundary layer thickness of the sliding manifold [21].

Substituting K_i and u_d into Eq. (15), we obtain

$$\begin{aligned} s\dot{s} = sC^{\mathrm{T}}B\Bigg\{ & \sum_{i=1}^{4}[(\alpha_i - \bar{\alpha}_i) - (\sup\ \alpha_i - \bar{\alpha}_i + \delta_i)sC^{\mathrm{T}}\bar{B}x_i/\lambda]x_i \\ & + [(\beta - \bar{\beta}) + (\gamma - \bar{\gamma})c_5 r_d] - [(\sup\ \beta - \bar{\beta}) + (\tilde{\gamma} - \bar{\gamma})c_5 r_d + \delta_d]sC^{\mathrm{T}}\bar{B}/\lambda \Bigg\}. \end{aligned} \tag{25}$$

Combining Eqs. (25) and (21) yields

$$\begin{aligned} s\dot{s} = \varepsilon\Bigg\{ & \sum_{i=1}^{4}[\alpha_i - \bar{\alpha}_i]sC^{\mathrm{T}}\bar{B}x_i + [(\beta - \bar{\beta}) + (\gamma - \bar{\gamma})c_5 r_d]sC^{\mathrm{T}}\bar{B} - \sum_{i=1}^{4}(\sup\ \alpha_i - \bar{\alpha}_i + \delta_i)(sC^{\mathrm{T}}\bar{B}x_i)^2\frac{1}{\lambda} \\ & - [(\sup\ \beta - \bar{\beta}) + (\tilde{\gamma} - \gamma)c_5 r_d + \delta_d](sC^{\mathrm{T}}\bar{B})\frac{1}{\lambda}\Bigg\}. \end{aligned} \tag{26}$$

One can see from the above equation that the reaching condition (14) is guaranteed if the following conditions are satisfied:

$$\left|sC^{\mathrm{T}}\bar{B}x_i\right| > \lambda, \quad i = 1,2,3,4, \tag{27}$$

$$\left|sC^{\mathrm{T}}\bar{B}\right| > \lambda. \tag{28}$$

Observe Eqs. (13), (22) and (23). One may see that the proposed control action will cancel the hysteresis effect and also achieve a cubic order state feedback. It is worth mentioning that the control action of Eq. (13) with parameters given in Eqs. (22) and (23) is continuous as long as the reference input r_d is a continuous signal. If the reference signal has discontinuity (e.g., a step input), the control action will correspondingly be discontinuous. However, in the overall control action shown in Eq. (13), the effect of reference input r_d only appears as a linear term (see Eq. (23)). Compared to the cubic state feedback (the first term in the right hand side of Eq. (13)), one may envision that the control action corresponding to a reference discontinuity will have a relatively small effect on the overall control action. This will be further illustrated in the simulations that follow. In comparison, the conventional IVSC [22,33] (see Appendix C) uses a linear state feedback and, as a result, the discontinuous effect will be more significant. In addition, the switching control also could play its role at this discontinuous point, i.e., attempting to confine the states within the boundary layer of the sliding manifold, which will intensify the discontinuity of control action. It is clear that the control action of ICSMC will be smoother than that of the conventional IVSC under the same discontinuous reference input. The detailed comparisons will be provided in the simulation section.

3.2. Manifold coefficients determination and tracking performance analysis

It is often recognized that $s = 0$ when the system enters the sliding manifold [22,31–33]. However, generally $s \neq 0$ because of the non-zero boundary layer thickness and the tracking error. Here we set $s = \delta(t)$, where $|\delta(t)|$ is less than the boundary layer thickness, when the system is confined within the boundary layer of sliding manifold. The system reaches the steady state when $\delta(t)$ approaches to a small constant value, e.g., δ^c. Combining Eqs. (9), (11) and (12), we obtain

$$\dot{\bar{x}} = A_{sm}\bar{x} + B_{sm}\begin{bmatrix} r_d \\ F_m \end{bmatrix}, \quad y = C_{sm}\bar{x}, \tag{29a,b}$$

where

$$\bar{x} = \begin{bmatrix} x_1 \\ x_2 \\ x_3 \\ z - \dfrac{c_4}{c_5}\delta^c \end{bmatrix}, \quad A_{sm} = \begin{bmatrix} 0 & 1 & 0 & 0 \\ -\dfrac{\hat{k}}{\hat{m}} & -\dfrac{\hat{g}}{\hat{m}} & -\dfrac{\hat{k}_1}{\hat{m}} & 0 \\ -\dfrac{c_1}{c_4} & -\dfrac{c_2}{c_4} & -\dfrac{c_3}{c_4} & -\dfrac{c_5}{c_4} \\ -\phi(\hat{l}) & 0 & 0 & 0 \end{bmatrix},$$

$$B_{sm} = \begin{bmatrix} 0 & 0 \\ 0 & \dfrac{1}{\hat{m}} \\ 0 & 0 \\ 1 & 0 \end{bmatrix}, \quad C_{sm} = [\,\phi(\hat{l}) \quad 0 \quad 0 \quad 0\,].$$

Clearly, the system dynamics within the boundary layer is determined by c_i, $i = 1, \ldots, 5$. The determination of c_i should lead to: (1) stability of (29) and (2) tracking performance and external disturbance attenuation capability.

In order to satisfy the stability requirement, the eigenvalues of matrix A should all have negative real parts. The standard pole placement approach can be employed to determinate the values of c_i, $i = 1, \ldots, 5$ [22,33]. Taking the Laplace transform of system (29) under zero initial conditions yields

$$\begin{aligned} Y(s) &= \frac{\frac{\hat{k}_1}{\hat{m}}\,\phi(\hat{l})\frac{c_5}{c_4}\,R_d(s) + \left(s^2 + \frac{c_3}{c_4}\,s\right)\frac{\phi(\hat{l})}{\hat{m}}\,F_m(s)}{s^4 + \left(\frac{\hat{g}}{\hat{m}} + \frac{c_3}{c_4}\right)s^3 + \left(\frac{\hat{k}}{\hat{m}} + \frac{\hat{g}}{\hat{m}}\frac{c_3}{c_4} - \frac{\hat{k}_1}{\hat{m}}\frac{c_2}{c_4}\right)s^2 + \left(-\frac{\hat{k}_1}{\hat{m}}\frac{c_1}{c_4} + \frac{\hat{k}}{\hat{m}}\frac{c_3}{c_4}\right)s + \frac{\hat{k}_1}{\hat{m}}\,\phi(\hat{l})\,\frac{c_5}{c_4}} \\ &= G_{r_d y}(s)R_d(s) + G_{F_m y}(s)F_m(s). \end{aligned} \tag{30}$$

The characteristic equation of the sliding mode dynamics is given as

$$s^4 + \left(\frac{\hat{g}}{\hat{m}} + \frac{c_3}{c_4}\right)s^3 + \left(\frac{\hat{k}}{\hat{m}} + \frac{\hat{g}}{\hat{m}}\frac{c_3}{c_4} - \frac{\hat{k}_1}{\hat{m}}\frac{c_2}{c_4}\right)s^2 + \left(-\frac{\hat{k}_1}{\hat{m}}\frac{c_1}{c_4} + \frac{\hat{k}}{\hat{m}}\frac{c_3}{c_4}\right)s + \frac{\hat{k}_1}{\hat{m}}\phi(\hat{l})\frac{c_5}{c_4} = 0. \tag{31}$$

Let the desired characteristic equation under the desired eigenvalues ω_i $(i = 1, \ldots, 4)$ be

$$\prod_{i=1}^{4}(s - \omega_i) = s^4 + \sigma_1 s^3 + \sigma_2 s^2 + \sigma_3 s + \sigma_4 = 0. \tag{32}$$

Comparing Eqs. (31) and (32), we obtain the following sliding manifold coefficients:

$$\frac{c_1}{c_4} = -\frac{\bar{k}}{\bar{k}_1}\left(\frac{\bar{g}}{\bar{m}} - \sigma_1\right) - \frac{\bar{m}}{\bar{k}_1}\sigma_3, \quad \frac{c_1}{c_4} = -\frac{\bar{m}}{\bar{k}_1}\,\sigma_2 + \frac{\bar{k}}{\bar{k}_1} - \frac{\bar{g}}{\bar{k}_1}\left(\frac{\bar{g}}{\bar{m}} - \sigma_1\right), \tag{33a,b}$$

$$\frac{c_3}{c_4} = -\frac{\bar{g}}{\bar{m}} + \sigma_1, \quad \frac{c_5}{c_4} = \frac{\bar{m}}{\bar{k}_1 \phi(l)}\,\sigma_4, \tag{33c,d}$$

where the over-bar indicates the nominal value of the corresponding parameter. Without loss of generality, we may set $c_4 = 1$, and the rest of c_i can be solved from Eq. (33).

When all the desired eigenvalues are placed in the left-hand side of the complex plane, the stability of Eq. (29) is guaranteed. In order to satisfy the tracking performance, we may use the final value theorem

$$\lim_{t\to\infty} y(t) = \lim_{s\to 0} sY(s) = \lim_{s\to 0} s[G_{r_d y}(s)R_d(s) + G_{F_m y}(s)F_m(s)]. \tag{34}$$

Assume that both the reference r_d and the external disturbance F_m are step signals. By virtue of Eq. (30), we have

$$\lim_{t\to\infty} y(t) = \lim_{s\to 0}\left[sG_{r_d y}(s)\,\frac{r_d}{s} + sG_{F_m y}(s)\,\frac{F_m}{s}\right] = r_d + 0F_m. \tag{35}$$

Clearly, we can achieve zero steady-state tracking error and completely reject the external disturbance for step signals.

The above analysis provides a theoretical explanation of system tracking and disturbance attenuation capability for special input and external disturbance (both being step signals). In practical situation, both input signal and external disturbance could be more complicated. It has been mentioned that once the system is confined in the sliding manifold, the performance will depend on the manifold design. From Eq. (30), one can see that the transfer function from inputs (for both reference signal and disturbance) to output is strictly proper. If the poles of Eq. (30) are placed in the open left-hand side of the complex plane, the magnitude of the transfer function after cutoff frequency will roll off. Typical transfer functions of the sliding manifold are illustrated in Fig. 7. In other words, the transfer function from the reference input signal to the output has low-pass filter characteristic, while the transfer function from the disturbance to output plays an attenuation role. These characteristics of sliding manifold are expected, because generally the tracked reference signal is in low-frequency band while the disturbance signal is in high-frequency band.

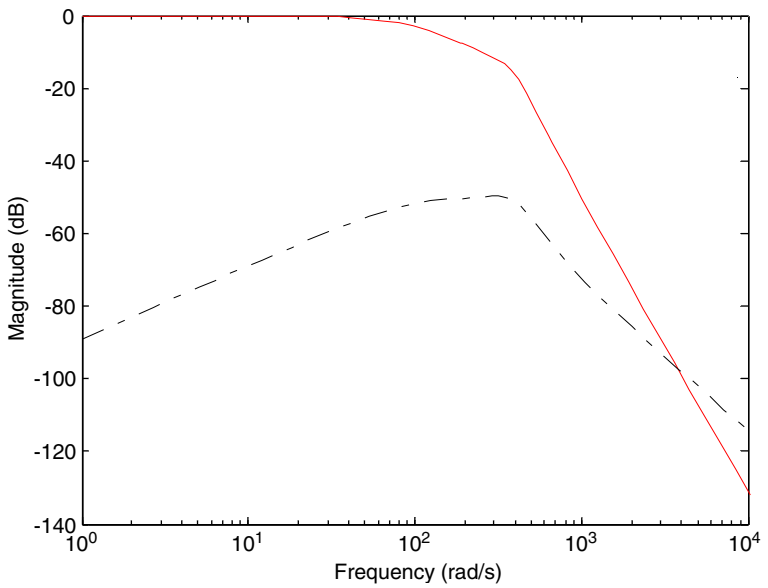

Fig. 7. Bode diagram of sliding manifold: ——, signal transfer function; — · —, disturbance transfer function.

4. Simulation results and discussion

In this section, we carry out analyses on the beam structure shown in Fig. 3 to illustrate the control design and demonstrate the system performance. We first compare the proposed ICSMC with a regular optimal control, to verify the hysteresis cancellation performance of the former. We then compare the ICSMC with conventional CSMC and IVSC under a variety of operating conditions to confirm the performance improvement in terms of tracking accuracy, robustness and control action smoothness. The system parameters used in the analyses are listed in Tables 1 and 2.

4.1. Comparison with respect to LQR on hysteresis compensation

If one uses a linear constitution relation for the piezoelectric actuator (such as the one shown in Eq. (4)), after introducing the shunt circuit one will end up with a linear system that is similar to the one described by Eq. (8) except that the nonlinear hysteresis effect $f(Q)$ does not appear. In that sense, one may treat the hysteresis effect in Eq. (8) as disturbance/noise, and resort to linear control algorithms such as linear optimal control (LQR) for control development. It is worth mentioning that the piezoelectric hysteresis could explicitly be treated as disturbance/noise, only after we introduce the shunt circuit. Meanwhile, using linear control algorithms is indeed a very natural choice in most of the applications so far, when one neglects the nonlinearity in piezoelectric constitutive relation. In order to illustrate the hysteresis effect and demonstrate the system performance improvement due to ICSMC, in this first case study we compare the proposed ICSMC with a conventional LQR where the hysteresis nonlinearity is not considered in control design and only treated as a disturbance. Here the reference signal is assumed to be a sinusoid signal. In order to obtain a fair comparison, we adjust the weightings in the LQR design so that the peak control voltage requirements for both controllers are the same under zero external excitations. The simulation results are shown in Fig. 8. Compared to the reference signal, the beam displacement exhibits a significant delay under LQR control, which is obviously caused by the hysteresis that is treated as a disturbance in the LQR design. ICSMC, on the

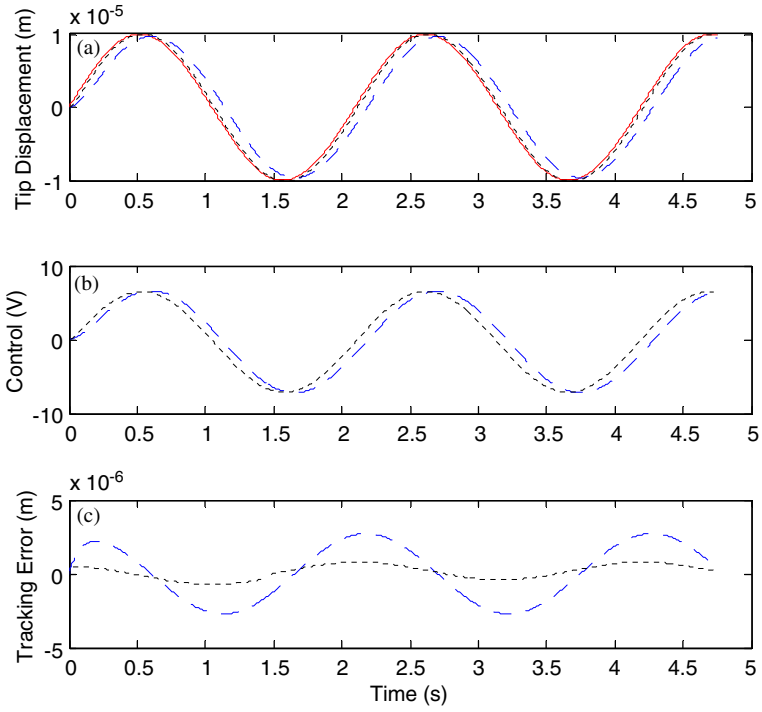

Fig. 8. Tracking control comparisons between LQG and ICSMC: (a) control performance, (b) control voltage, (c) error, ———, reference signal;– – –, LQG;--------, ICSMC.

other hand, leads to a very fast controlled response and much reduced delay, due to the hysteresis compensation explicitly incorporated into the control development as well as the cubic feedback. Most importantly, ICSMC significantly reduces the tracking error. As shown in Fig. 8, ICSMC has a 10% peak tracking error as compared to the 25% tracking error under LQR. This example clearly shows the negative effect of piezoelectric hysteresis under linear system assumption, and demonstrates the necessity of hysteresis compensation for high-precision control.

4.2. Comparison with respect to CSMC and IVSC on robustness and control action smoothness

One important feature of the proposed ICSMC is that it has improved tracking performance and control action smoothness as compared to other nonlinear controls such as CSMC and IVSC. In what follows we demonstrate the performance improvement in this regard. We assume the system described by Eq. (8) has the following bounds of uncertainties due to modeling error:

$$|\Delta m| \leqslant m \times 10\%, \quad |\Delta g| \leqslant g \times 10\%, \quad |\Delta k| \leqslant k \times 10\%, \quad |\Delta k_1| \leqslant k_1 \times 10\%,$$

$$|\Delta L| \leqslant L \times 10\%, \quad |\Delta R| \leqslant R \times 10\%, \quad |\Delta k_2| \leqslant k_2 \times 10\%, \quad |\Delta k_3| \leqslant k_3 \times 10\%.$$

In all following case studies, the piezoelectric hysteresis is modeled and included in control development and in the analyses. We also assume that the bounds for the parameters related to the hysteresis modeling (listed in Table 1) are 20%.

The detailed derivation of CSMC approach is outlined in Appendix B. The control parameters of CSMC (listed in Table 3) are chosen in a manner such that the system can follow the command step signal when external disturbance is absent. Here the reference input is a step signal with magnitude rising from 0 to 10 μm at 0.1 s. We then apply an external disturbance that is also a step signal with magnitude rising from 0 to 100 μN at 2.5 s. The control result under CSMC is shown in Fig. 9. Clearly, the beam tip displacement can indeed follow the command signal from 0 to 2.5 s when the external disturbance is absent. Once the external step disturbance is imposed onto the system, however, CSMC fails to eliminate the tracking error. The control voltage input is also illustrated in Fig. 9. Corresponding to the reference signal step-up, the control input has a very large jump at 0.1 s. In practical situation, the control input voltage will saturate before it reaches such large magnitude. Under the assumption that the saturation voltage is ± 80 V, the control result is shown in Fig. 10. Obviously the chattering phenomenon is present due to the saturation of control input voltage, and the system performs very badly. This second case study clearly demonstrates the limitation of CSMC in terms of the command signal tracking under disturbance.

It is generally recognized that IVSC is suitable for robust tracking control [22,33]. In the third case study, we compare the proposed ICSMC with IVSC (see Appendix C for derivations) under various operating conditions. In order to obtain a fair comparison, we use the same coefficients of sliding manifolds for both controllers. The other control parameters are selected in such a manner that the control voltage input and tip displacement of ICSMC are very close to those of IVSC under the condition that both reference input and

Table 3
Parameters of CSMC

Parameter	Value	Parameter	Value	Parameter	Value
$\bar{\alpha}_1$	-6.5813×10^7	δ_1	0.1	inf γ	-8.8485×10^7
$\bar{\alpha}_2$	3.6869×10^4	δ_2	0.1	$\bar{\tau}$	-4.1234×10^5
$\bar{\alpha}_3$	2.9569×10^8	δ_3	0.1	sup τ	-3.7110×10^5
$\bar{\alpha}_4$	2.6307×10^5	δ_4	0.1	inf τ	-4.5357×10^5
sup α_1	-4.8459×10^7	δ_d	0.1	c_1	5418.9
sup α_2	4.0644×10^4	$\bar{\beta}$	1.4764	c_2	1.4623
sup α_3	3.9934×10^8	sup β	2.9528	c_3	3497.8
sup α_4	2.8999×10^5	$\bar{\gamma}$	-6.8472×10^7	c_4	1
λ	8.1×10^{-4}	sup γ	-4.8459×10^{-4}		

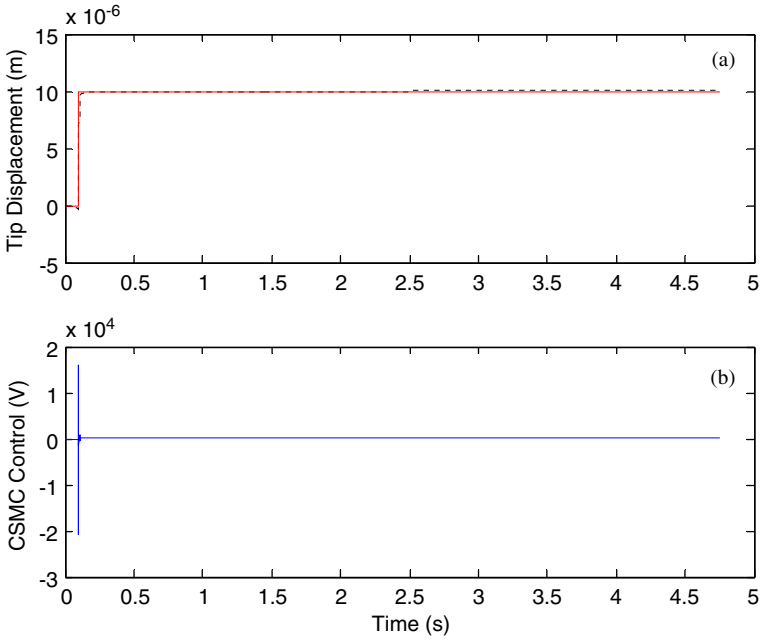

Fig. 9. CSMC result under step reference input and step external disturbance without considering the saturation of control input voltage: (a) control performance, (b) control voltage; ———, reference signal; ---------, CSMC.

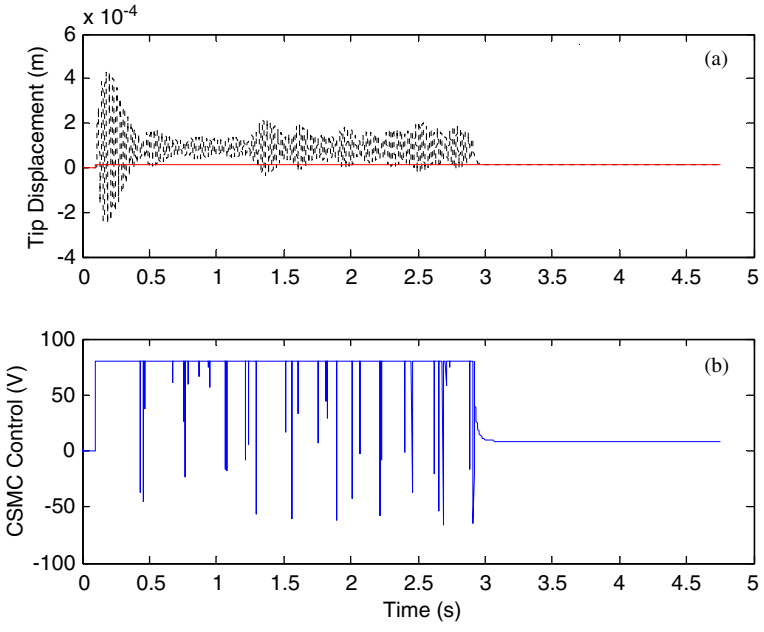

Fig. 10. CSMC result under step reference input and step external disturbance with control input voltage saturation: (a) control performance, (b) control voltage; ———, reference signal; --------, CSMC.

external disturbance are step signals. The control parameters are listed in Tables 4 and 5, respectively. The reference signal and disturbance situation are the same as assumed in the previous case study.

From Fig. 11, we can see that both IVSC and ICSMC can follow the step command input and reject the external step disturbance. Further inspection of the control voltage input (shown in Fig. 12) shows that IVSC

Table 4
Parameters of IVSC

Parameter	Value	Parameter	Value	Parameter	Value
c_1	23.174	c_4	1	ξ_0	20
c_2	1.2	c_5	−3959.7	ξ_1	100
c_3	3581.8	η	42688		

Table 5
Parameters of ICSMC

Parameter	Value	Parameter	Value	Parameter	Value
$\bar{\alpha}_1$	-4.8345×10^6	λ	10^{-5}	$\bar{\gamma}$	76.092
$\bar{\alpha}_2$	1.5651×10^3	δ_1	0.1	sup γ	83.702
$\bar{\alpha}_3$	2.4198×10^8	δ_2	0.1	inf γ	68.483
$\bar{\alpha}_4$	2.6946×10^5	δ_3	0.1	c_1	23.174
sup α_1	-3.5498×10^6	δ_4	0.1	c_2	1.2
sup α_2	1.7937×10^3	δ_d	0.1	c_3	3581.8
sup α_3	3.2713×10^8	$\bar{\beta}$	1.2119	c_4	1
sup α_4	2.9702×10^5	sup β	2.4237	c_5	−3959.7

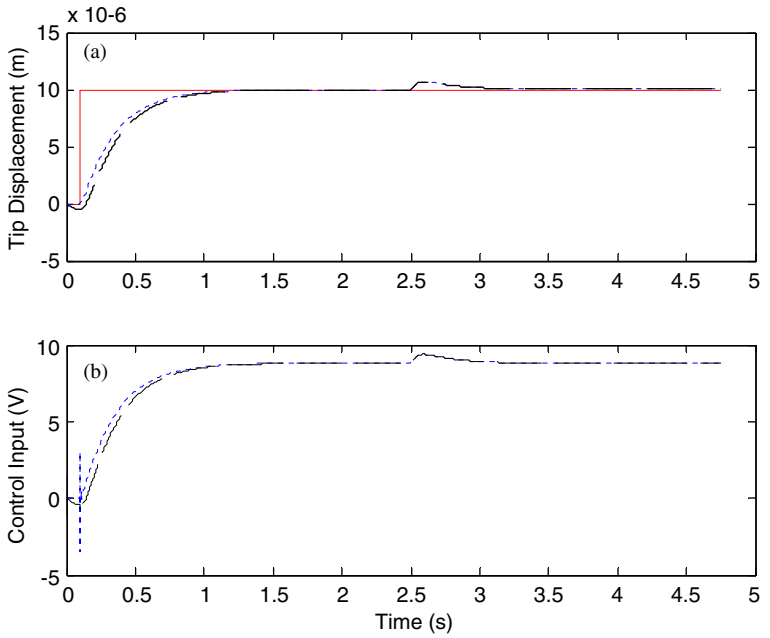

Fig. 11. IVSC and ICSMC comparison: (a) control performance, (b) control voltage; ———, reference signal; --------, IVSC; – – –, ICSMC.

exhibits control voltage sudden change at 0.1 s when the command signal has a sudden jump. It is worth mentioning that in the IVSC design, we have already incorporated a modified proper continuous function to alleviate the chattering phenomenon [22]. The current simulation is under single mode discretization, and thus the sudden and drastic change of control voltage does not lead to significant tracking performance deterioration. Nevertheless, it can be envisioned that in practical implementation where the beam has infinitely

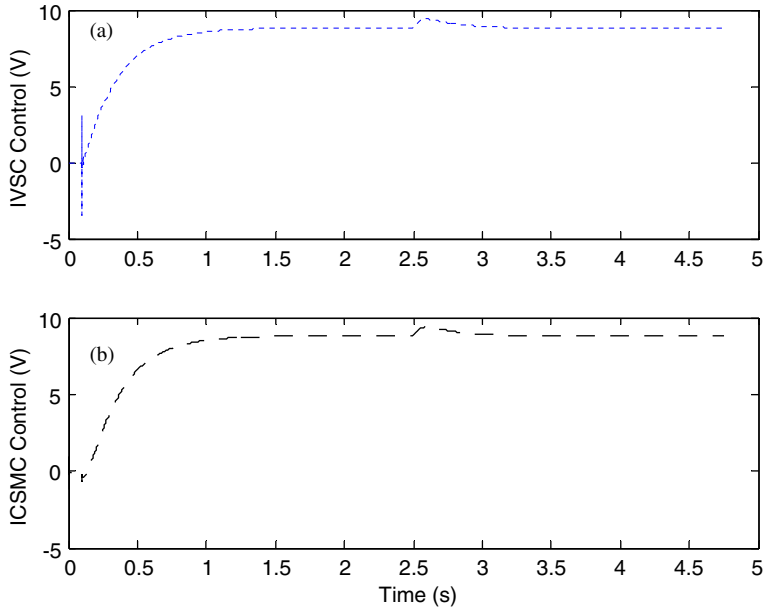

Fig. 12. Control voltage comparison: (a) IVSC, (b) ICSMC; --------, IVSC; ———, ICSMC.

many degrees of freedom, such voltage chattering would trigger the high frequency un-modeled dynamics. The control action of ICSMC, on the other hand, is much smoother than that of IVSC as expected. At 0.1 s, the control voltage of ICSMC still exhibits a small discontinuity due to the reference jump. However, the magnitude is very small as compared to that of IVSC. After a step external disturbance is imposed onto the system at 2.5 s, both IVSC and ICSMC can eliminate the tracking error and their control voltage inputs are similar.

Fig. 13 illustrates a square wave tracking control comparison between IVSC and ICSMC. A Gaussian random is added to the system as an external disturbance. Both IVSC and ICSMC can follow the square wave. Once again, the control input of IVSC shows large jumps at changing edges of square wave. Close inspection of the beam tip displacement shows that ICSMC has better control robustness as compared to IVSC under the same random disturbance. In order to more clearly demonstrate the random disturbance attenuation, we present another case study in Fig. 14, where the reference input is set to be zero and the system is under Gaussian random disturbance. This is a typical case of vibration suppression. It is obvious from Fig. 14 that ICSMC has much improved disturbance attenuation capability than IVSC, which is due to the cubic state feedback that can respond faster and more effective at early stage when the beam tip is disturbed away from the zero position. Fig. 15 illustrates another beam vibration attenuation comparison. In this case, an initial velocity is imposed on beam tip, and external disturbance is still Gaussian random noise. Both IVSC and ICSMC show good vibration attenuation capability, but the result of ICSMC is better than that of IVSC. ICSMC has smaller over-shoot and requires less time to reach steady state.

5. Conclusion

In this research, a robust and high precision control methodology is developed for a piezoelectric actuator with hysteresis compensation. An RL shunt circuit is introduced to the piezoelectric actuator to form an actuator network, which leads to two coupled dynamic sub-systems that can be cast into standard state-space format for control development. With this actuator circuit configuration, the charge and/or current in the piezoelectric actuator now become independent state variables that can be measured and fed back, which enables a direct hysteresis compensation.

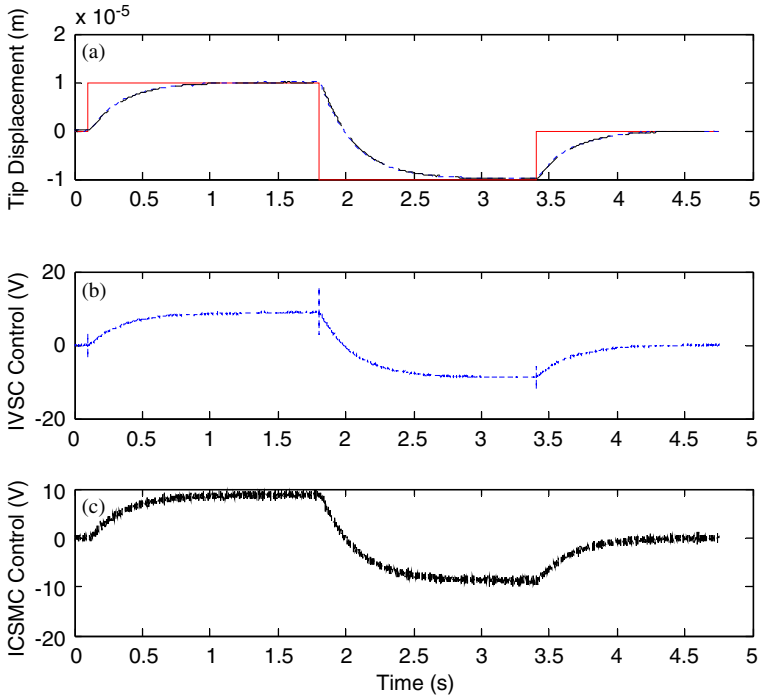

Fig. 13. Square wave tracking result comparison between IVSC and ICSMC: (a) control performance, (b) IVSC control voltage, (c) ICSMC control voltage; ———, reference signal; – – –, IVSC; -------, ICSMC.

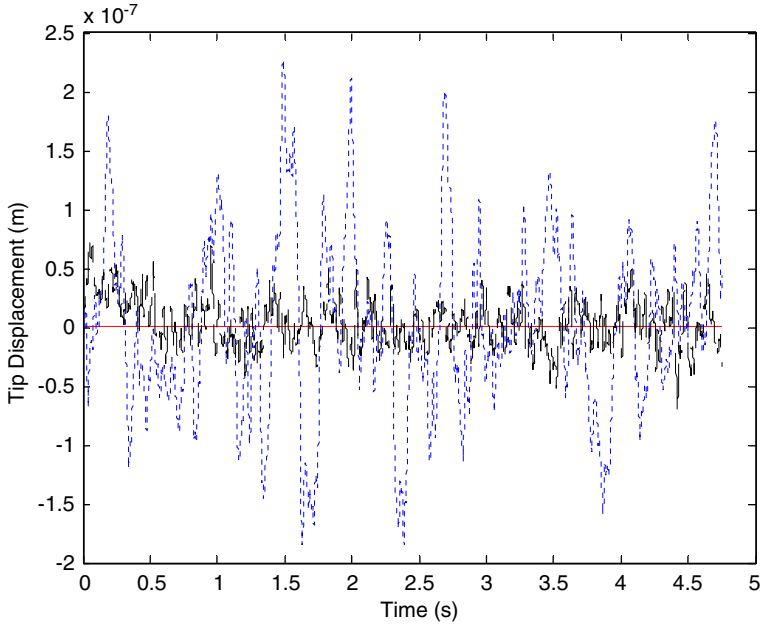

Fig. 14. Comparison of random disturbance attenuation between IVSC and ICSMC ———: reference signal; ---------: IVSC; – – –, ICSMC.

An ICSMC scheme, which combines the advantages of conventional CSMC and IVSC, is then developed and analyzed. It is shown that this ICSMC algorithm leads to much improved control precision as compared to LQR when piezoelectric hysteresis is present. This comparison clearly demonstrates the necessity of

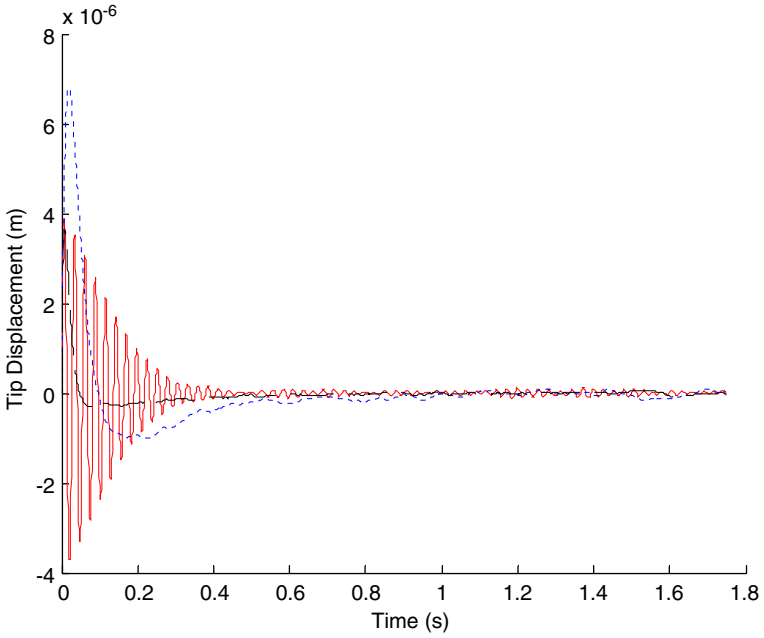

Fig. 15. Comparison of free vibration attenuation between IVSC and ICSMC: ———, uncontrolled; --------, IVSC; – – –, ICSMC.

hysteresis compensation. Analyses are also provided to illustrate the improved tracking control and vibration attenuation accuracy, enhanced control robustness under external disturbance, and better control action smoothness of the proposed ICSMC as compared to conventional CSMC and IVSC.

Acknowledgment

This research is partially supported by the National Science Foundation under Grant CMS—0428210, by the University of Connecticut Research Foundation, and by the NASA EPSCoR Program through Connecticut Space Grant College Consortium.

Appendix A. Dynamic equations of beam structure integrated with piezoelectric actuator

The equations of motion of a beam subject to piezoelectric actuator control (Fig. 3) can be derived using the Hamilton's principle. Following the procedure outlined in Ref. [20], we have

$$\int_{t_1}^{t_2} [\delta T_b + \delta T_p - \delta U_b - \delta U_p + \delta W_v]\,\mathrm{d}t = 0, \tag{A.1}$$

where subscript "b" and "p" refer to beam and piezoelectric actuator, respectively. T, U_b, U_p and δW_v are, respectively, the kinetic energy of the integrated system, the potential energy of the beam, the elastic and electrical energy of the piezoelectric actuator, and the virtual work term.

Using Eqs. (8a) and (8b) and beam theory, we have

$$T = T_b + T_p = \tfrac{1}{2} m_b \dot{q}^2 + \tfrac{1}{2} m_p \dot{q}^2, \tag{A.2}$$

$$U_b = \tfrac{1}{2} k_b q^2, \tag{A.3}$$

where

$$m_b = \int_0^{l_b} \rho_b A_b \phi(x)^2\,\mathrm{d}x, \quad m_p = \int_0^{l_b} \rho_p A_p \phi(x)^2 \Delta H\,\mathrm{d}x, \quad k_b = \int_0^{l_b} E_b I_b [\partial^2 \phi(x)/\partial x^2]^2\,\partial x. \tag{A.4}$$

Here, $\Delta H = H(x - x_l) - H(x - x_r)$, and $H(x)$ is the Heavyside step function. All relevant notations are listed in the nomenclature.

The electrical displacement D of the piezoelectric patch is discretized as

$$D = \psi p. \tag{A.5}$$

Using the constitutive relation (7a,b), the elastic and electrical energy variation of the piezoelectric actuator can be obtained as

$$\begin{aligned}\delta U_p &= \int_V (T\delta s + E\delta D)\mathrm{d}V \\ &= \int_V [(\bar{c}_{11}^D s - h_{31}D)\delta s + (-g_{31}(\bar{c}_{11}^D + \bar{c}_{12}^D)s + 2h_{31}g_{31}D + \{\beta_{33}^{\mathrm{T}}D\})\delta D]\mathrm{d}V \\ &= k_p q\delta q + k_{pq}p\delta q + k_{p\varepsilon}q\delta p + k_{pD}p\delta p + A_p h_p \psi\{\beta_{33}^{\mathrm{T}}D\}\delta p,\end{aligned} \tag{A.6}$$

where

$$\begin{aligned}k_p &= \int_0^{l_b} \bar{c}_{11}^D I_{pz}\left[\frac{\partial^2\phi(x)}{\partial x^2}\right]\Delta H\,\mathrm{d}x, \\ k_{pq} &= \int_0^{l_b} F_p h_{31}\left(\frac{\partial^2\phi(x)}{\partial x^2}\right)\psi\Delta H\,\mathrm{d}x, \\ k_{p\varepsilon} &= \int_0^{l_b} F_p g_{31}(\bar{c}_{11}^D + \bar{c}_{12}^D)\left[\frac{\partial^2\phi(x)}{\partial x^2}\right]\psi\Delta H\,\mathrm{d}x, \\ k_{pD} &= \int_0^{l_b} A_p(2h_{31}g_{31})\psi^2\Delta H\,\mathrm{d}x.\end{aligned} \tag{A.7}$$

Three terms are involved in the virtual work, i.e., the voltage across the piezoelectric actuator, the external disturbance, and the beam structure damping:

$$\delta W_{\mathrm{v}} = F_e\delta p + F_m\delta q - g\dot{q}\delta q, \tag{A.8}$$

where

$$F_e = \int_0^{l_b} V_a w_p\psi\Delta H\,\mathrm{d}x,\quad F_m = \int_0^{l_b} F(x,t)\phi(x)\,\mathrm{d}x,\quad g = \int_0^{l_b} c_b\phi(x)^2\,\mathrm{d}x. \tag{A.9}$$

Substituting the kinetic energy, potential energy and virtual work into Eq. (A.7), assuming that the electrical displacement is independent of the spatial coordinates, i.e., $\psi = 1$, and assuming $D = Q/A_p$, we have

$$m\ddot{q} + g\dot{q} + kq + k_1 Q = F_m, \tag{A.10}$$

$$k_2 Q + k_3 q + h_p\left\{\beta_{33}^{\mathrm{T}}\frac{Q}{h_p l_p}\right\} = V_a, \tag{A.11}$$

where

$$m = m_b + m_p,\quad k = k_b + k_p,\quad k_1 = \frac{k_{pq}}{A_p},\quad k_2 = \frac{k_{pD}}{(A_p)^2},\quad k_3 = \frac{k_{p\varepsilon}}{A_p}. \tag{A.12}$$

After we introduce the resistance/inductance shunt circuit, the system equation becomes

$$m\ddot{q} + g\dot{q} + kq + k_1 Q = F_m, \tag{A.14}$$

$$L\ddot{Q} + R\dot{Q} + k_2 Q + k_3 q + h_p\left\{\beta_{33}^{\mathrm{T}}\frac{Q}{h_p l_p}\right\} = V_i. \tag{A.15}$$

Appendix B. Continuous sliding mode control (CSMC) design

The derivation is similar to that of ICSMC. Let

$$\bar{z} = [\phi(l)x_1, x_2, x_3, x_4]^{\mathrm{T}}. \tag{B.1}$$

Then Eq. (9) can be re-written as

$$\dot{\bar{z}} = A_z\bar{z} - Bf(x_3) + Bu + DF_m, \tag{B.2}$$

where

$$A_z = \begin{bmatrix} 0 & \phi(l) & 0 & 0 \\ -\dfrac{k}{m}\dfrac{1}{\phi(l)} & -\dfrac{g}{m} & -\dfrac{k_1}{m} & 0 \\ 0 & 0 & 0 & 1 \\ -\dfrac{k_3}{L}\dfrac{1}{\phi(l)} & 0 & -\dfrac{k_2}{L} & -\dfrac{R}{L} \end{bmatrix}. \tag{B.3}$$

We define the sliding manifold as

$$s = C^{\mathrm{T}}\bar{z} - c_1 r_d. \tag{B.4}$$

Let the control input be

$$u = -K\tilde{z} + \hat{f}(x_3) - u_d, \tag{B.5}$$

where

$$\tilde{z} = [\bar{z}_1 - r_d, \bar{z}_2, \bar{z}_3, \bar{z}_4]^{\mathrm{T}}. \tag{B.6}$$

Applying the reaching condition (14), and using Eqs. (B.2) and (B.3), we have

$$s\dot{s} = sC^{\mathrm{T}}[A_z\bar{z} - Bf(x_3) + Bu + DF_m] - c_1\dot{r}_d. \tag{B.7}$$

Substituting Eq. (B.5) into Eq. (B.7) yields

$$s\dot{s} = sC^{\mathrm{T}}B\{[\alpha - K]\tilde{z} + [\beta + \gamma r_d + \tau\dot{r}_d - u_d]\}, \tag{B.8}$$

where

$$\alpha = (C^{\mathrm{T}}B)^{-1}C^{\mathrm{T}}A_z = [\alpha_1, \alpha_2, \alpha_3, \alpha_4], \tag{B.9}$$

$$\beta = (C^{\mathrm{T}}B)^{-1}C^{\mathrm{T}}DF_m + \Delta f, \tag{B.10}$$

$$\gamma = -(C^{\mathrm{T}}B)^{-1}C^{\mathrm{T}}E, \quad \tau = -(C^{\mathrm{T}}B)^{-1}c_1, \tag{B.11,B12}$$

$$E = \left[0, \frac{k}{m}\frac{1}{\phi(l)}, 0, \frac{k_3}{L}\frac{1}{\phi(l)}\right]^{\mathrm{T}}, \quad \Delta f = \hat{f}(x_3) - f(x_3). \tag{B.13,B.14}$$

Here we define

$$\bar{\tau} = \frac{\sup\,\tau + \inf\,\tau}{2}. \tag{B.15}$$

In order to satisfy the reaching condition (14), we may choose the following control parameters:

$$K_i = \bar{\alpha}_i + (\sup\,\alpha_i - \bar{\alpha}_i + \delta_i)\frac{sC^{\mathrm{T}}\bar{B}\tilde{z}_i}{\lambda}, \quad \delta_i > 0, \quad i = 1, 2, 3, 4, \tag{B.16}$$

$$u_d = \bar{\beta} + \bar{\gamma}c_5 r_d + \{[\sup\,\beta - \bar{\beta}] + (\tilde{\gamma} - \bar{\gamma})r_d + (\tilde{\tau} - \bar{\tau})\dot{r}_d + \delta_d\}\frac{sC^{\mathrm{T}}\bar{B}}{\lambda}, \quad \delta_d > 0, \tag{B.17}$$

where

$$\tilde{\gamma} = \begin{cases} \sup\ \gamma & \text{when } r_d > 0, \\ \inf\ \gamma & \text{when } r_d < 0, \end{cases} \tag{B.18}$$

$$\tilde{\tau} = \begin{cases} \sup\ \tau & \text{when } \dot{r}_d > 0, \\ \inf\ \tau & \text{when } \dot{r}_d < 0, \end{cases} \tag{B.19}$$

λ is again the boundary layer thickness of the sliding manifold.

Substituting Eqs. (B.16) and (B.17) into Eq. (B.8), we obtain

$$\begin{aligned} s\dot{s} = \varepsilon \Bigg\{ & \sum_{i=1}^{4} [\alpha_i - \bar{\alpha}_i] s C^{\mathrm{T}} \bar{B} \tilde{z}_i + [(\beta - \bar{\beta}) + (\gamma - \bar{\gamma}) r_d + (\tau - \bar{\tau}) \dot{r}_d] s C^{\mathrm{T}} \bar{B} \\ & - \sum_{i=1}^{4} (\sup\ \alpha_i - \bar{\alpha}_i + \delta_i)(s C^{\mathrm{T}} \bar{B} \tilde{z}_i)^2 \frac{1}{\lambda} - [(\sup\ \beta - \bar{\beta}) + (\tilde{\gamma} - \gamma) r_d + (\tilde{\tau} - \bar{\tau}) \dot{r}_d + \delta_d](s C^{\mathrm{T}} \bar{B}) \frac{1}{\lambda} \Bigg\}. \end{aligned} \tag{B.20}$$

Observe Eqs. (B.16) and (B.17). Clearly, if the following conditions are satisfied, the reaching condition (14) can be guaranteed:

$$\left| s C^{\mathrm{T}} \bar{B} x_i \right| > \lambda, \quad i = 1, 2, 3, 4, \tag{B.21}$$

$$\left| s C^{\mathrm{T}} \bar{B} \right| > \lambda. \tag{B.22}$$

The sliding manifold (B.4) can be derived using a similar pole placement procedure outlined in Section 3.2.

Appendix C. Integral variable structure control (IVSC) design

The classical design of IVSC involves the reaching mode and the sliding mode. By virtue of Eqs. (12) and (9), we have

$$\begin{aligned} \dot{s} &= C^{\mathrm{T}}[Ax - Bf(x_3) + Bu + DF_m] + c_5[r_d - \phi(l) x_1] \\ &= [C^{\mathrm{T}} A - A_\phi] x - C^{\mathrm{T}} B f(x_3) + C^{\mathrm{T}} B u + C^{\mathrm{T}} D F_m + c_5 r_d z. \end{aligned} \tag{C.1}$$

In what follows we let the control input be decomposed into the equivalent control input u_{eq} and the switching control input u_s:

$$u = u_{\mathrm{eq}} + u_s. \tag{C.2}$$

The equivalent control input is defined as the solution of $\dot{s} = 0$ under conditions that both the external disturbance and the uncertainties are absent:

$$u_{\mathrm{eq}} = -(C^{\mathrm{T}} \bar{B})^{-1} [(C^{\mathrm{T}} \bar{A} - A_\phi) x + c_5 r_d] + \hat{f}(x_3). \tag{C.3}$$

The switching part is used primarily for satisfying the reaching condition and also for overcoming the external disturbance and the uncertainties. When the trajectory of the system is in the vicinity of the sliding manifold, the switching part of the controller constraines the system to follow the sliding manifold. In theory, the sign discontinuous function can be used as the switching control action [31,32]. However, the control action triggered by the sign function is in the high frequency band and can lead to the chattering phenomenon and excite the high frequency un-modeled dynamics of the system [22]. In order to alleviate the chattering phenomenon, the sign function is generally replaced by a proper continuous function, which is further improved by using a modified proper continuous function to account for different operating conditions [22]:

$$u_s = -\eta M_\xi(s), \tag{C.4}$$

where

$$M_{\xi}(s) = \frac{s}{|s| + \xi_0 + \xi_1|\phi(l)x_1 - r_d|}. \tag{C.5}$$

Here ξ_0 and ξ_1 are positive constants.

It can be easily verified that when the constant switching gain η is chosen in the following manner the reaching condition (14) can be guaranteed:

$$\eta = \sum_{i=1}^{4}(\sup\, a_i)|x_i| + \sup\, \Delta f + (\sup\, \Delta D)|F_m| + (\sup\, \Delta B)|r_d|, \tag{C.6}$$

where

$$\Delta A = (C^{\mathrm{T}}\bar{B})^{-1}(C^{\mathrm{T}}\bar{A} - A_{\phi}) - [C^{\mathrm{T}}B]^{-1}[C^{\mathrm{T}}A - A_{\phi}] = [a_1, a_2, a_3, a_4], \tag{C.7}$$

$$\Delta B = \{(C^{\mathrm{T}}\bar{B})^{-1} - [C^{\mathrm{T}}B]^{-1}\}c_5, \tag{C.8}$$

$$\Delta D = [C^{\mathrm{T}}B]^{-1}C^{\mathrm{T}}D. \tag{C.9}$$

The sliding manifold can be derived using a similar pole placement procedure outlined in Section 3.2.

References

[1] A.F. Devonshire, Theory of ferroelectrics, *Advances in Physics* 3 (10) (1954) 85–130.

[2] J. Sirohi, I. Chopra, Fundamental understanding of piezoelectric strain sensors, *Journal of Intelligent Material Systems and Structures* 11 (4) (2000) 246–257.

[3] T.G. King, M.E. Preston, B.J.M. Murphy, D.S. Cannel, Piezoelectric ceramic actuators: a review of machinery applications, *Precision Engineering* 12 (3) (1990) 131–136.

[4] I. Mayergoyz, *Mathematical Models of Hysteresis*, Springer, New York, 1991.

[5] P. Ge, M. Jouaneh, Modeling hysteresis in piezoceramic actuators, *Precision Engineering* 17 (3) (1995) 211–221.

[6] P. Ge, M. Jouaneh, Generalized Preisach model for hysteresis nonlinearity of piezoceramic actuators, *Precision Engineering* 20 (3) (1997) 99–111.

[7] M. Goldfarb, N. Celanovic, A lumped parameter electrochemical model for describing the nonlinear behavior of piezoelectric actuators, *ASME Journal of Dynamic Systems, Measurement, and Control* 119 (1997) 478–485.

[8] M. Goldfarb, N. Celanovic, Modeling piezoelectric stack actuator for control of micromanipulation, *IEEE Control System Magazine* 17 (3) (1997) 69–79.

[9] S.-H. Lee, T.J. Royston, Modeling piezoceramic transducer hysteresis in the structural vibration control problem, *Journal of Acoustic Society of America* 108 (6) (2000) 2843–2855.

[10] S. Chonan, Z. Jiang, T. Yamamoto, Nonlinear hysteresis compensation of piezoelectric ceramic actuators, *Journal of Intelligent Material Systems and Structures* 7 (1996) 150–156.

[11] M.-S. Tsai, J.-S. Chen, Robust tracking control of a piezoactuator using a new approximate hysteresis model, *ASME Journal of Dynamic Systems, Measurement, and Control* 125 (2003) 96–102.

[12] P. Ge, M. Jouaneh, Tracking control of a piezoceramic actuator, *IEEE Transactions on Control Systems Technology* 4 (1996) 209–216.

[13] J.A. Main, E. Garcia, Piezoelectric stack actuators and control system design: strategies and pitfalls, *Journal of Guidance, Control, and Dynamics* 20 (1997) 479–485.

[14] Y.-S. Kung, R.-F. Fung, Precision control of a piezoceramic actuator using neutral networks, *ASME Journal of Dynamic Systems, Measurement, and Control* 126 (2004) 235–238.

[15] D. Croft, S. Devasia, Hysteresis and vibration compensation for piezoactuators, *Journal of Guidance, Control, and Dynamics* 21 (1998) 710–717.

[16] G.S. Choi, Y.A. Lim, G.H. Choi, Tracking position control of piezoelectric actuators for periodic reference inputs, *Mechatronics* 12 (2002) 669–684.

[17] T. Chang, X. Sun, Analysis and control of monolithic piezoelectric nano-actuator, *IEEE Transactions on Control Systems Technology* 9 (1) (2001) 69–75.

[18] J. Tang, K.W. Wang, High authority and nonlinearity issues in active–passive hybrid piezoelectric networks for structural damping, *Journal of Intelligent Material Systems and Structures* 11 (3) (2000) 581–591.

[19] S.-H. Lee, M.B. Ozer, T.J. Royston, Piezoceramic hysteresis in the adaptive structural vibration control problem, *Journal of Intelligent Material Systems and Structures* 13 (2002) 117–124.

[20] J. Tang, K.W. Wang, Active–passive hybrid piezoelectric networks for vibration control: comparisons and improvement, *Smart Materials and Structures* 10 (2001) 794–806.

[21] F. Zhou, D.G. Fisher, Continuous sliding mode control, *International Journal of Control* 55 (2) (1992) 313–327.

[22] T.-L. Chern, Y.-C. Wu, Design of integral variable structure controller and application to electrohydraulic velocity servosystems, *IEE Proceedings-D* 138 (5) (1991) 439–444.
[23] P. Chen, S. Montgomery, A macroscopic theory for the existence of the hysteresis and butterfly loops in ferroelectricity, *Ferroelectrics* 23 (1980) 199–207.
[24] Standards Committee of the IEEE Ultrasonics, Ferroelectrics, and Frequency Control Society, *An American National Standard: IEEE Standard on Piezoelectricity, The Institute of Electrical and Electronics Engineers, ANSI/IEEE Std* 176-1987, New York, 1987.
[25] J.A. Main, E. Garcia, Design impact of piezoelectric actuator nonlinearities, *Journal of Guidance, Control, and Dynamics* 20 (1997) 327–332.
[26] J.A. Main, E. Garcia, D.V. Newton, Precision position control of piezoelectric actuators using charge feedback, *Journal of Guidance, Control, and Dynamics* 18 (1995) 1068–1073.
[27] D. Damjanovic, Stress and frequency dependence of the direct piezoelectric effect in ferroelectric ceramics, *Journal of Applied Physics* 82 (1997) 1788–1797.
[28] D.V. Taylor, D. Damjanovic, Evidence of domain wall contribution to the dielectric permittivity in PZT thin films at sub-switching fields, *Journal of Applied Physics* 82 (1997) 1973–1975.
[29] D. Damjanovic, R.E. Newnham, Electrostrictive and piezoelectric materials for actuator applications, *Journal of Intelligent Material Systems and Structures* 3 (1992) 190–208.
[30] M.S. Tsai, K.W. Wang, On the structural damping characteristic of active piezoelectric actuators with passive shunt, *Journal of Sound and Vibration* 221 (1) (1999) 1–22.
[31] J.Y. Hung, W. Gao, J.C. Hung, Variable structural control: a survey, *IEEE Transactions on Industrial Electronics* 40 (1) (1993) 2–22.
[32] V.I. Utkin, Sliding mode control design principle and applications to electrical drives, *IEEE Transactions on Industrial Electronics* 40 (1) (1993) 23–36.
[33] C.-C. Cheng, I.-M. Liu, Design of MIMO integral variable structure controllers, *Journal of The Franklin Institute* 336 (1999) 1119–1134.
[34] D.J. Davison, A. Goldenberg, Robust control of general servomechanism problem: the servo compensator, *Automatica* 11 (1975) 461–471.